Available online at www.sciencedirect.com
ScienceDirect
Journal of Power Sources 161 (2006) 308–322
JOURNAL OF POWER SOURCES
www.elsevier.com/locate/jpowsour

Experimental and modeling study of solid oxide fuel cell operating with syngas fuel

R. Suwanwarangkul [a], E. Croiset [a,*], E. Entchev [b], S. Charojrochkul [c], M.D. Pritzker [a], M.W. Fowler [a], P.L. Douglas [a], S. Chewathanakup [c], H. Mahaudom [c]

[a] *Department of Chemical Engineering, University of Waterloo, Waterloo, Ont., Canada N2L 3G1*
[b] *Advanced Combustion Technologies Laboratory, CANMET Energy Technology Centre, 1 Haanel Drive, Ottawa, Ont., Canada K1A 1M1*
[c] *Department of Ceramic Technology, National Metals and Materials Technology Center, 114 Thailand Science Park, Paholyothin Road., Klongluang, Pathumthani 12120, Thailand*

Received 25 January 2006; received in revised form 29 March 2006; accepted 29 March 2006
Available online 7 July 2006

Abstract

A two-dimensional isothermal model of an SOFC operating with a syngas fuel based on button cell geometry was developed. Momentum, mass and charge transport coupled with electrochemical and chemical reactions were considered. The developed model has been validated by showing good agreement with experimental data for various syngas compositions obtained at an operating temperature of 900 °C. However, the model predictions deviate somewhat from the experimental data at 800 °C. Visual and SEM investigation of the anode surface after completion of each experiment showed that excessive amounts of carbon form on the anode surface and that the Ni catalyst delaminates from the anode during cell operation at 800 °C. In contrast, no carbon formation was observed and only a small amount of Ni delaminated from the anode during operation at 900 °C. The model was further applied to predict carbon formation observed experimentally, and to study the impact of operating conditions on carbon formation and determine a suitable range of conditions that suppress its onset.

Keywords: Solid oxide fuel cell; Mathematical modeling; Syngas fuel; Model validation; CO–H_2 electrochemical reactions; Water-gas shift reaction

1. Introduction

With the rising concern about greenhouse gas emissions, many countries are pursuing efforts to develop more sustainable energy systems to replace conventional combustion heat engines. Solid oxide fuel cell (SOFC) power generation shows great promise to serve as an alternative in the near future. Since SOFC operation relies on electrochemical reactions, its electrical efficiency is not limited by temperature as in the case of conventional heat engines. Therefore, the electrical efficiency obtained from a SOFC is typically greater and more stable than that obtained from conventional heat engines [1,2]. Furthermore, additional efficiency can be gained by incorporating a steam/gas turbine cycle to recover heat from the hot gas exhausted from SOFCs because they operate at high temperatures between 800 and 1000 °C [1]. Fuel flexibility with SOFCs also presents advantages over other types of fuel cells such as polymer electrolyte membrane fuel cells (PEMFCs). Not only is the carbon monoxide present in the fuel gas not harmful to SOFCs, but it can also act as a fuel. Therefore, a variety of hydrocarbon-based fuels or their syngas derivatives, such as natural gas, biomass and coal, can efficiently be used in SOFCs.

Biomass and coal are gasified to form syngas, essentially containing a mixture of H_2, CO, CO_2, H_2O, N_2 and eventually H_2S. This syngas can then be used as a fuel in SOFC. However, H_2S must be scrubbed before the syngas is fed to the SOFC to prevent rapid degradation of the SOFC performance [1]. Depending on the type of coal and biomass, the composition of syngas varies widely and affects the SOFC performance [3–8]. Also, carbon formation is a problem that can limit SOFC performance when used with syngas. This is due to the Boudouard reaction which converts CO to carbon on the anode surface:

$$2CO \rightarrow C + CO_2 \quad (1)$$

* Corresponding author. Tel.: +1 519 888 4567x6472; fax: +1 519 746 4979.
E-mail address: ecroiset@cape.uwaterloo.ca (E. Croiset).

0378-7753/$ – see front matter © 2006 Elsevier B.V. All rights reserved.
doi:10.1016/j.jpowsour.2006.03.080

Nomenclature

c	concentration (mol m^{-3})
D_{ij}	binary diffusivity of species i in species j (m^2 s^{-1})
D_{i-M}	binary diffusivity of species i in multi-component gaseous mixture (m^2 s^{-1})
E^0	ideal half-cell cell potential (V)
F	Faraday's constant (96487 A s mol^{-1})
I_{avg}	average current density (A m^{-2})
J	current density (A m^{-2})
k_{WGSR}	reaction rate constant for the water gas shift reaction
K_{eq}	equilibrium constant
M	molecular weight (g mol^{-1})
p	pressure (Pa)
r	radial coordinate (m)
R	gas constant (8.31441 J mol^{-1} K^{-1})
$R_{contact}$	contact resistance (Ω m^{-2})
R_{WGSR}	flux caused by WGSR (mol m^{-2} s^{-1})
s	interface conductivity for electrochemical reaction (Ω^{-1} m^{-2})
T	operating temperature (K)
u, v	velocity components in r and z directions, respectively (m s^{-1})
$V_{delivered}$	cell potential delivered to the load (V)
z	axial coordinate (m)

Greek letters

α_C	carbon activity for the Boudouard reaction defined in Eq. (23)
η	overpotential (V)
μ	viscosity (kg m^{-1} s^{-1})
ρ	gas density (kg m^{-3})
σ_e	ionic conductivity (Ω^{-1} m^{-1})
ϕ	potential (V)
ϕ_{an}, ϕ_{cat}	half-cell potential at the anode and the cathode, respectively (V)

Subscripts

an	anode
B	Boudouard reaction
cat	cathode
e	electrolyte
f	fuel channel
i	fuel gas species (H_2, H_2O, CO, CO_2 and N_2)
WGSR	water-gas shift reaction

Therefore, various operating strategies to suppress carbon formation must be devised. Faced with these potential problems, it is important to develop a model to predict SOFC performance for various operating conditions, in particular, syngas feed composition. Such a model could also be used to study the influence of these operating conditions on carbon formation.

In this paper, a mechanistic SOFC transport model coupled with electrochemical (H_2 oxidation, CO oxidation and O_2 reduction) and chemical reaction (water-gas shift) kinetics for syngas operation (mixtures of H_2, H_2O, CO, CO_2 and N_2) based on a button cell geometry is developed. A unique advantage of this model is that it accounts for electrochemical H_2 and CO oxidation. The developed model is validated using experimental cell performance data obtained for various syngas compositions at 800 and 900 °C. Visual and SEM investigation of the anode surface after cell operation at each operating temperature is performed. The model is also applied to predict carbon formation observed during experiments and then employed to study the influence of operating conditions on carbon deposition.

2. Experimental

The electrochemical cell used in this study was an Electrolyte Supported Cell (ESC) supplied by Innovative Dutch Electro Ceramics InDEC B.V. Co. Ltd. The ESC consists of a TZ3Y electrolyte (3 mol% yttria-stabilized zirconia) that is approximately 150 μm thick and fabricated by tape casting. A 60 μm thick Ni–CeO_2-YSZ anode and a 50 μm thick $La_{0.7}Sr_{0.2}MnO_{3-\delta}$ (LSM) cathode were screen printed on each side of the electrolyte. The cross-sectional areas of the electrolyte and each electrode are 25 cm^2 (5 cm × 5 cm) and 16 cm^2 (4 cm × 4 cm), respectively.

A schematic of the test rig is illustrated in Fig. 1. The anode part of the ESC was placed on a Ni mesh current collector spot-welded to two Ni wires acting as current and voltage probes. Both the Ni mesh and the ESC were fixed by a high temperature glass seal to the top of a quartz tube which was in turn attached to a stainless steel sample holder by a ceramic seal. The diameter of the quartz tube was 45 mm i.d. with 3 mm thickness. Two smaller quartz tubes (6 mm diameter) with different lengths were fixed to the sample holder using high temperature ceramic seals. The long tube was used for gas inlet while the shorter one served as the tube for gas outlet. The gas feed tube was located 4–5 mm away from the cell to ensure that the reactant gas was uniformly distributed over the entire area of the cell. On the cathode side, another quartz tube was placed on the cell to press the glass seal when it melted. This ensured that the glass seal fused to the cell and no leak occurred. The cathode part was directly exposed to ambient air so that air flowed to the cell via natural convection. A platinum mesh (Alfar Aesar Co. Ltd.) was used as the current collector at the cathode. A weight of 500 g was placed on top of the platinum mesh to ensure that it was in good contact with the cathode. This also helped reduce contact resistance between the platinum mesh and the ESC. A highly porous alumina layer was placed between the weight and the platinum mesh to allow the oxidant (oxygen) to reach the cathode reaction site underneath the weight uniformly. The cell test rig was contained inside a temperature-controlled furnace (Carbolite Co. Ltd.) to ensure that it could be operated under isothermal conditions. Two thermocouples were located at the vicinity of the anode and the cathode.

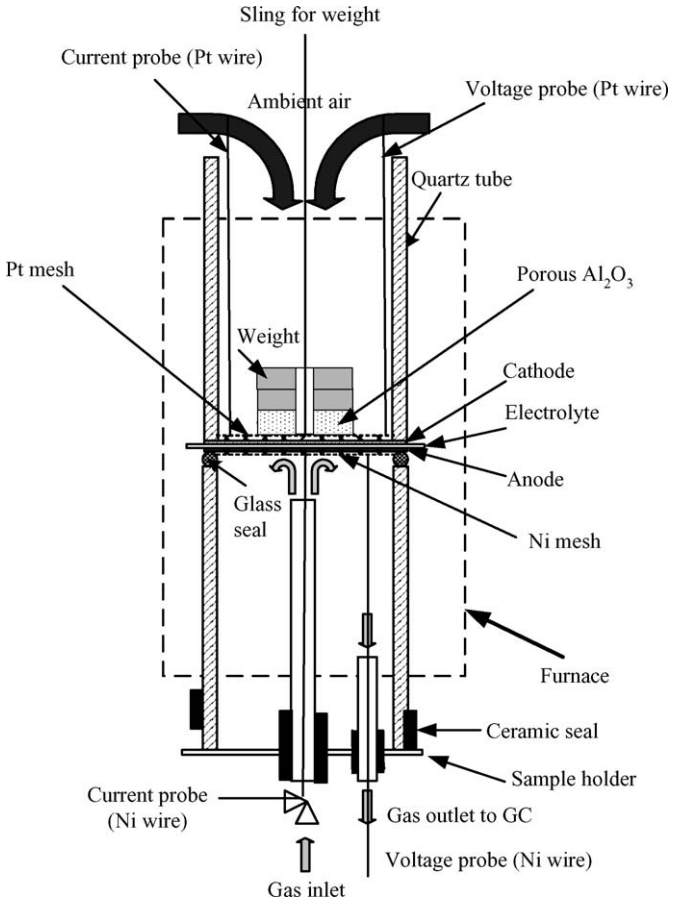

Fig. 1. Schematic diagram of test rig set up.

During the operation of the experimental set-up, H_2, CO, CO_2 and N_2 were mixed together using a set of mass flow controllers (Omega Co. Ltd.). The gas mixture was then passed through a flame arrester and a hydrator prior to entering the anode side of the electrochemical cell. A hydrator placed on a temperature-controlled bath was used to humidify the inlet gas stream. The extent of gas humidification was controlled by the bath temperature. The exit gas from the anode side was vented to the atmosphere through a fume hood. The inlet and exit lines were connected to a gas chromatograph (GC) to measure gas compositions.

The cell performance was characterized by measuring the cell potential as a function of the current density for various gas compositions, gas flow rates and operating temperatures. The cell potential and current were recorded only after the response had maintained a steady state for at least 3 min after the imposition of each load resistance setting. The load resistance was varied from high to low values corresponding to a range from low to high currents drawn from the cell. In these experiments, the influences of N_2 and CO_2 dilution, H_2/CO composition ratio and simulated syngas composition (mixture of H_2, CO, CO_2 and N_2) on cell performance were investigated. The operating temperatures for these experiments were 800 and 900 °C. After each experiment, the anode surface was inspected visually and by scanning electron microscope (SEM) to observe any change in the anode microstructure and any eventual carbon formation.

3. Mathematical modeling

3.1. Model geometry and assumptions

The geometry of the test rig is based on a button cell design including an anode feed tube, air channel, fuel channel and electrochemical cell. Due to symmetry conditions, only the portion of the rig shown in Fig. 2 is considered in the model using two-dimensional cylindrical coordinates (radial and vertical directions r and z). Fuel gas is supplied through the anode feed tube. Once it reaches the anode, it flows radially outward along the porous anode layer where it participates in the electrochemical and the water-gas shift reaction (WGSR) reactions. Gas is discharged from the cell by flowing from the anode layer into the gas outlet channel. Since the cathode is directly exposed to the ambient air within the furnace, no feed tube is required.

Assumptions used in this model development are as follows:

(a) Temperature is uniform over the entire model geometry. This assumption is reasonable because the test rig is small and is placed in a controlled-temperature furnace. Although heat is generated by the electrochemical reactions, temperature only slightly increases since the electrode area is relatively small and so heat generation is not significant.
(b) Gas density is constant because the temperature is uniform and the generation and consumption rates of gas species are low.
(c) Mass transport and ohmic resistances within the anode and the cathode are neglected since their thicknesses are very thin. This assumption is based on the work of Chan et al. [9]. Therefore, electrode subdomains are ignored in the model. Only the ohmic resistance through the electrolyte layer is considered in the model because the ionic conductivity is much less than the electronic conductivity of the electrodes.
(d) The electrochemical reactions and the WGSR occur exclusively at the electrode/electrolyte interfaces.

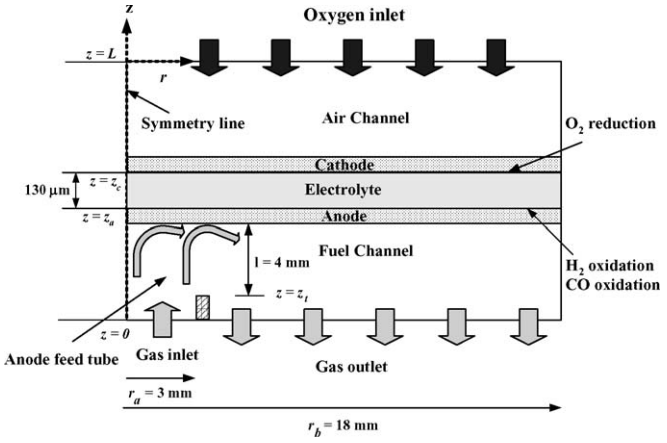

Fig. 2. Model geometry of the test rig (not to scale).

Table 1
List of governing equations[a]

Subdomain	Transport equation	
Fuel channel	Variables: v_f, u_f, p_f and c_i	
Overall mass	$\frac{\partial v_f}{\partial z} + \frac{1}{r}\frac{\partial (r u_f)}{\partial r} = 0$	(2)
Momentum z direction	$\frac{\rho \partial (v_f v_f)}{\partial z} + \frac{1}{r}\frac{\rho \partial (r u_f v_f)}{\partial r} = -\frac{\partial p_f}{\partial z} + \frac{\partial}{\partial z}\left(\mu_f \frac{\partial v_f}{\partial z}\right) + \frac{1}{r}\frac{\partial}{\partial r}\left(r\mu_f \frac{\partial v_f}{\partial r}\right) + \frac{\partial}{\partial z}\left(\mu_f \frac{\partial v_f}{\partial z}\right) + \frac{1}{r}\frac{\partial}{\partial r}\left(r\mu_f \frac{\partial u_f}{\partial z}\right)$	(3)
Momentum r direction	$\frac{\rho \partial (v_f u_f)}{\partial z} + \frac{1}{r}\frac{\rho \partial (r u_f u_f)}{\partial r} = -\frac{\partial p_f}{\partial r} + \frac{\partial}{\partial z}\left(\mu \frac{\partial u_f}{\partial z}\right) + \frac{1}{r}\frac{\partial}{\partial r}\left(r\mu_f \frac{\partial u_f}{\partial r}\right) + \frac{\partial}{\partial z}\left(\mu_f \frac{\partial v_f}{\partial r}\right) + \frac{1}{r}\frac{\partial}{\partial r}\left(r\mu_f \frac{\partial u_f}{\partial r}\right) - \frac{2\mu_f u_f}{r^2}$	(4)
Species	$\frac{\partial (c_i v_f)}{\partial z} + \frac{1}{r}\frac{\partial (r c_i u_f)}{\partial r} = \frac{\partial}{\partial z}\left(D_{i-M}\frac{\partial c_i}{\partial z}\right) + \frac{1}{r}\frac{\partial}{\partial r}\left(r D_{i-M}\frac{\partial c_i}{\partial r}\right)$	(5)
Electrolyte	Variable: ϕ_e	
Ion	$\frac{1}{r}\frac{\partial (r\partial\phi_e/\partial r)}{\partial r} + \frac{\partial^2 \phi_e}{\partial z^2} = 0$	(6)
Air channel	Variable: c_{O_2}	
Oxygen	$\frac{\partial}{\partial z}\left(D_{O_2-N_2}\frac{\partial c_{O_2}}{\partial z}\right) + \frac{1}{r}\frac{\partial}{\partial r}\left(r D_{O_2-N_2}\frac{\partial c_{O_2}}{\partial r}\right) = 0$	(7)

[a] Where i are H_2, H_2O, CO and CO_2, u_f and v_f are the fuel velocities in r and z directions, respectively, p_f the pressure field within fuel channel, c_i the concentration of ith species, D_{i-M} the binary diffusivity of ith species in multi-component mixture, φ_e the potential within the electrolyte subdomain layer, c_{O_2} the partial pressure of O_2 and $D_{O_2-N_2}$ is the binary diffusivity of O_2–N_2 system.

3.2. Governing equations

The governing equations are summarized in Table 1. The Navier-Stokes equations [10] and mass transport equations [11] within the fuel channel are solved simultaneously to determine the velocity of the fuel stream and concentration profile of each

Table 2
List of operating conditions and model input parameters

Item	Value
Operating conditions	
Pressure (Pa)	1 atm (101.35 kPa)
Temperature	800 and 900 °C
Fuel flow rate	100–180 ml min^{-1}
Fuel gas composition	Vary
Cell potential ($\phi_{cat} - \phi_{an}$)	0.5–1.0 V
Oxidant	Air
Model input parameters	
Conductivity of the electrolyte (σ_e, Ω^{-1} m^{-1})	2.26 at 800 °C, 5.12 at 900 °C
Equilibrium and kinetic constants	
K_{eq,H_2} (atm$^{-0.5}$)	1.78×10^9 at 800 °C, 1.66×10^8 at 900 °C
$K_{eq,CO}$ (atm$^{-0.5}$)	1.63×10^9, 1.07×10^8
$K_{eq,WGSR}$	1.04, 0.75
k_{WGSR} (mol m^{-2} atm^{-2} s^{-1})	1.6×10^8, 4.3×10^8
Binary diffusion coefficients (cm^2 s^{-1})	
$D_{H_2-H_2O}$	7.68 at 800 °C, 8.94 at 900 °C
D_{H_2-CO}	6.45, 7.47
$D_{H_2-CO_2}$	8.67, 10.0
$D_{H_2-N_2}$	6.36, 7.38
D_{H_2O-CO}	2.22, 2.58
$D_{H_2O-CO_2}$	1.71, 2.01
$D_{H_2O-N_2}$	2.19, 2.58
D_{CO-CO_2}	1.41, 1.62
D_{CO-N_2}	1.74, 2.04
$D_{CO_2-N_2}$	1.38, 1.62
$D_{O_2-N_2}$	1.83, 2.07

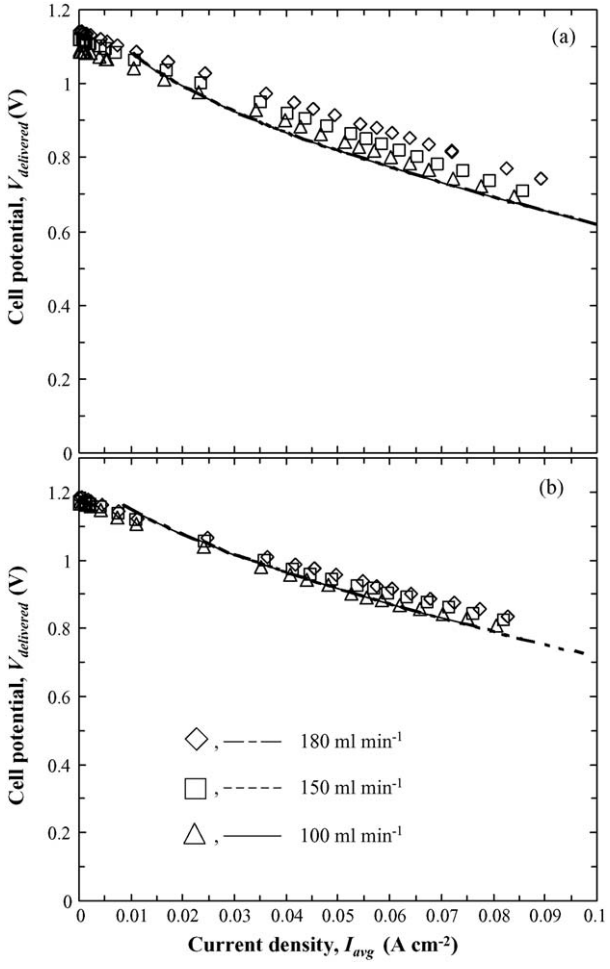

Fig. 3. Experimental (symbols) and predicted (lines) cell performances at various fuel flow rates at (a) 800 °C and (b) 900 °C using H_2 as fuel.

gas species. Fuel gases considered in the model are H_2, CO, CO_2, H_2O and N_2. Only charge transport [12] is considered within the electrolyte subdomain layer to calculate the potential distribution and calculate the ohmic overpotential. Mass transport and ohmic resistances within the porous electrode layers are ignored. Only mass transport of O_2 is considered within the air channel. Electrochemical and chemical reactions considered in this model are O_2 reduction at the cathode, H_2 and CO oxidation at the anode, and the WGSR at the anode/electrolyte interface, which are described in detail next.

3.3. Electrochemical reactions

Electrochemical reactions are coupled with the transport equations to determine the distributions of the local current density and electrode overpotentials inside the SOFC. They are specified here as boundary conditions at the electrode/electrolyte interfaces. In reality, electrochemical reactions in an SOFC take place at the triple phase boundaries (TPB) between the ionic conductor, electronic conductor and gas in the vicinity of electrode/electrolyte interface where O^{2-} and electrons meet [13]. Important aspects and the rate expressions of these reactions are summarized in this section.

3.3.1. Oxygen reduction reaction

The rate of oxygen reduction at the cathode

$$O_2 + 4e^- \rightarrow 2O^{2-} \tag{8}$$

varies depending on the cathode and electrolyte materials as well as on the temperature. For conventional cathode material (LSM), the dissociation of adsorbed oxygen molecules is the rate-determining step (Minh and Takahashi, 1995). Therefore, the rate expression for oxygen reduction at an SOFC cathode is based on this step.

The rate of O_2 reduction at the cathode is determined by the rate of O_2 adsorption as the rate-determining step [14] and is given by [15]

$$J_{\text{cat}} = \frac{0.25 \times 10^{10} \times \exp(-130000/RT) RT p_{\text{O}_2,\text{cat}}^{0.50}}{F} \times \left\{ \exp\left(\frac{-2F\eta_{\text{cat}}}{RT}\right) - \exp\left(\frac{2F\eta_{\text{cat}}}{RT}\right) \right\} \tag{9}$$

where $p_{\text{O}_2,\text{cat}}$ is the partial pressure of oxygen at the cathode. η_{cat} is the activation overpotential for O_2 reduction defined as

$$\eta_{\text{cat}} = \phi_{\text{cat}} - \phi_{\text{e}}(r, z_{\text{c}}) - E^0_{\text{cat}} \tag{10}$$

where ϕ_{cat} and $\phi_{\text{e}}(r, z_{\text{c}})$ represent the cathode and electrolyte potentials, respectively, at the cathode/electrolyte interface. E^0_{cat} is the reversible potential for O_2 reduction:

$$E^0_{\text{cat}} = \left(\frac{RT}{4F}\right) \ln p_{\text{O}_2,\text{cat}} \tag{11}$$

3.3.2. H_2 and CO oxidation reactions

Various mathematical expressions for the rate of H_2 oxidation

$$H_2 + O^{2-} \rightarrow H_2O + 2e^- \tag{12}$$

on a conventional anode (Ni-YSZ) have been proposed [13–17]. The rate expression for H_2 oxidation at the anode used in this work is adopted from [15] and is given by

$$J_{\text{H}_2,\text{an}} = \frac{RT}{3F} s_{\text{H}_2,\text{an}} \left\{ \exp\left(\frac{2F\eta_{\text{H}_2,\text{an}}}{RT}\right) - \exp\left(\frac{-F\eta_{\text{H}_2,\text{an}}}{RT}\right) \right\} \tag{13}$$

where $s_{\text{H}_2,\text{an}}$ and $\eta_{\text{H}_2,\text{an}}$ are the anode interface conductivity ($\Omega^{-1}\,\text{m}^{-2}$) and activation overpotential (V) for H_2 oxidation, respectively. $s_{\text{H}_2,\text{an}}$ is estimated using the following empirical correlation:

$$s_{\text{H}_2,\text{an}} = 6.2 \times 10^{11} \times \exp\left(\frac{-120000}{RT}\right) \left(\frac{p_{\text{H}_2\text{O}}}{K_{\text{eq},\text{H}_2} p_{\text{H}_2}}\right)^{0.266} \tag{14}$$

where K_{eq,H_2} is the equilibrium constants for the reaction $H_2 + 1/2O_2 \rightarrow H_2O$. Substitution of Eq. (14) into Eq. (13) yields the following rate expression for H_2 oxidation:

$$J_{\text{H}_2,\text{an}} = \frac{2.1 \times 10^{11} \times \exp(-120000/RT) p_{\text{H}_2\text{O}}^{0.266} RT}{(K_{\text{eq},\text{H}_2} p_{\text{H}_2})^{0.266} F} \times \left\{ \exp\left(\frac{2F\eta_{\text{H}_2,\text{an}}}{RT}\right) - \exp\left(\frac{-F\eta_{\text{H}_2,\text{an}}}{RT}\right) \right\} \tag{15}$$

where $\eta_{\text{H}_2,\text{an}}$ is defined as

$$\eta_{\text{H}_2,\text{an}} = \phi_{\text{an}} - \phi_{\text{e}}(r, z_{\text{a}}) - E^0_{\text{H}_2,\text{an}} \tag{16}$$

and ϕ_{an} and $\phi_{\text{e}}(r, z_{\text{a}})$ represent the anode and electrolyte potentials, respectively, at the anode/electrolyte interface. $E^0_{\text{H}_2,\text{an}}$ is the reversible potential for H_2 oxidation:

$$E^0_{\text{H}_2,\text{an}} = \left(\frac{RT}{2F}\right) \ln\left(\frac{p_{\text{H}_2\text{O}}}{K_{\text{eq},\text{H}_2} p_{\text{H}_2}}\right) \tag{17}$$

Although the reaction mechanisms and rate expression of CO oxidation

$$CO + O^{2-} \rightarrow CO_2 + 2e^- \tag{18}$$

have been less studied than that of H_2 oxidation, it is believed that the rate-determining step for CO oxidation is similar to that for H_2 oxidation [13]. Setoguchi et al. [18] found that the anodic interface conductivity for CO oxidation ($s_{\text{CO},\text{an}}$) is the same as that of H_2 oxidation if the partial pressure of O_2 during H_2 oxidation is similar to that during CO oxidation. This suggests that the interface conductivity of CO oxidation can be described by a similar correlation to that of H_2 oxidation, i.e.,

$$s_{\text{CO},\text{an}} = 6.2 \times 10^{11} \times \exp\left(\frac{-120000}{RT}\right) \left(\frac{p_{\text{CO}_2}}{K_{\text{eq},\text{CO}} p_{\text{CO}}}\right)^{0.266} \tag{19}$$

where $K_{\text{eq},\text{CO}}$ is the equilibrium constants for the reaction $CO + 1/2O_2 \rightarrow CO_2$.

However, it was recently found that CO oxidation has a much higher overpotential than H_2 oxidation for the same current density and the difference cannot be attributed to differences in concentration overpotential [19]. This observation agrees with

that of Matzusaki et al. [20] who found the rate of CO oxidation to be 2–3 times less than that of H_2 oxidation over the entire range of overpotential and the same partial pressure of O_2. Based on this argument, the rate of CO oxidation reaction used in this model development is assumed to be 2.5 times less than that for H_2 oxidation reaction, i.e., $J_{CO,an} = 0.4 J_{H_2,an}$. Accordingly, the rate expression for CO oxidation is expressed as

$$J_{CO,an} = \frac{0.84 \times 10^{11} \times \exp(-120000/RT) p_{CO_2}^{0.266} RT}{(K_{eq,CO} p_{CO})^{0.266} F} \times \left\{ \exp\left(\frac{2F\eta_{CO,an}}{RT}\right) - \exp\left(\frac{-F\eta_{CO,an}}{RT}\right) \right\} \quad (20)$$

where $\eta_{CO,an}$ is defined as

$$\eta_{CO,an} = \phi_{an} - \phi_e(r, z_a) - E^0_{CO,an} \quad (21)$$

and $E^0_{CO,an}$ is the ideal anode half-cell potential for CO oxidation reaction as given by

$$E^0_{CO,an} = \left(\frac{RT}{2F}\right) \ln\left(\frac{p_{CO_2}}{K_{eq,CO} p_{CO}}\right) \quad (22)$$

3.4. Chemical reactions

3.4.1. Water-gas shift reaction (WGSR)

Due to its high operating temperature, nickel can act as a catalyst for the WGSR at the anode when syngas is used as a fuel source. The rate expression R_{WGSR} for this reaction is written as [20,21]

$$R_{WGSR} = k_{WGSR}\left(p_{H_2O} p_{CO} - \frac{p_{H_2} p_{CO_2}}{K_{eq,WGSR}}\right) \quad (23)$$

where k_{WGSR} is the rate constant and $K_{eq,WGSR}$ the equilibrium constant for the WGSR. The following expression for k_{WGSR} can be obtained by fitting an Arrhenius curve to the experimental data given in [21]:

$$k_{WGSR} = 1.71 \times 10^8 \times \exp\left(-\frac{103191}{RT}\right) \quad (24)$$

The temperature dependence of $K_{eq,WGSR}$ is given by

$$K_{eq,WGSR} = \exp(-0.2935Z^3 + 0.6351T^3 + 4.1788Z + 0.3169) \quad (25)$$

where $Z = \frac{1000}{T(K)} - 1$

Since the rate of the WGSR is quite high, the WGSR has been assumed be at thermodynamic equilibrium in various SOFC models [13,21–24]. However, Ahmed and Föger [25] reported that the WGSR reaches very close to equilibrium only at high levels of fuel utilization ($U_f \sim 80$–100%). The actual extent of reaction was only about 80–90% of the equilibrium level at lower fuel utilization ($U_f \sim 0$–0.80). Therefore, in this model, we do not assume that the WGSR has reached equilibrium and instead consider that its rate is given by Eq. (23).

3.4.2. Carbon formation reaction

Carbon formation is undesirable since it can impede gas flow and block active sites on the anode. In addition, it can result in the growth of carbon filaments that generate massive forces within the electrode structure which can cause rapid catalyst breakdown [26]. Therefore, it is important to understand the kinetics of carbon formation and determine the conditions to suppress its formation. For syngas-fed SOFCs, carbon formation most likely occurs through the Boudouard reaction, as indicated in Eq. (1), since Ni is a good catalyst for this reaction. The reaction mechanism and kinetic expression for the Boudouard reaction on Ni-supported YSZ have not been well established. However, it is believed that this reaction is fast enough to attain equilibrium. Accordingly, in previous studies, a thermodynamic analysis of carbon formation rather than a kinetic analysis has been considered to determine suitable operating conditions such as feed composition, temperature and pressure to suppress carbon deposition [14,26–29]. We adopt a similar approach in this study and do not incorporate carbon formation directly into the model for cell performance.

Based on the thermodynamics of the Boudouard reaction, carbon can form when

$$\alpha_C = K_{eq,B} p_{CO}^2 / p_{CO_2} > 1 \quad (26)$$

where $K_{eq,B}$ is the equilibrium constant of the Boudouard reaction, which decreases as the operating temperature rises. The ratio, α_C, is sometimes referred to, more or less correctly, as "carbon activity". The possibility of carbon formation can be obtained from the solution of the fuel cell model that determines values of p_{CO} and p_{CO_2} at positions along the anode. The value of α_C at each position is then assessed according to the criterion given in Eq. (26) to determine whether carbon formation is thermodynamically possible.

3.5. Boundary conditions

In order to solve the system of equations, boundary conditions are specified at all the outer interfaces of the computational domains, the anode/electrolyte ($0 < r < r_b$, $z = z_a$), the cathode/electrolyte interfaces ($0 < r < r_b$, $z = z_c$) and at the anode tube wall ($r = r_a$, $0 < z < z_t$). At the fuel inlet ($0 < r < r_a$, $z = 0$), the inlet velocity and fuel gas mole fractions are prescribed while the inlet mole fraction of O_2 is specified at the air inlet ($0 < r < r_b$, $z = L$). At the fuel outlet ($r_a < r < r_b$, $z = 0$), only the operating pressure is prescribed, i.e., $p_f = 1.013 \times 10^5$ Pa; for all other variables, the gradients in the flow direction are assumed to be zero, i.e., $\partial v_f/\partial z = 0$, $\partial u_f/\partial z = 0$, $\partial c_i/\partial z = 0$. Along the symmetry line at $r = 0$, the following conditions hold: $\partial p_f/\partial r = 0$, $\partial v_f/\partial r = 0$, $\partial u_f/\partial r = 0$ and $\partial c_i/\partial r = 0$. At the anode/electrolyte interface at $z = z_a$, the fuel velocities in the radial and vertical directions are zero, i.e., $u_f = v_f = 0$. The flux of each gas species is related to the rate of H_2 or CO oxidation according to Faraday's law and the WGSR kinetics: $\vec{N}_{H_2} = -D_{H_2}\partial c_{H_2}/\partial z = R_{WGSR} - J_{H_2,an}/2F$, $\vec{N}_{H_2O} = J_{H_2,an}/2F - R_{WGSR}$, $\vec{N}_{CO} = -J_{CO,an}/2F - R_{WGSR}$, and $\vec{N}_{CO_2} = J_{CO,an}/2F + R_{WGSR}$. The charge flux is related to the

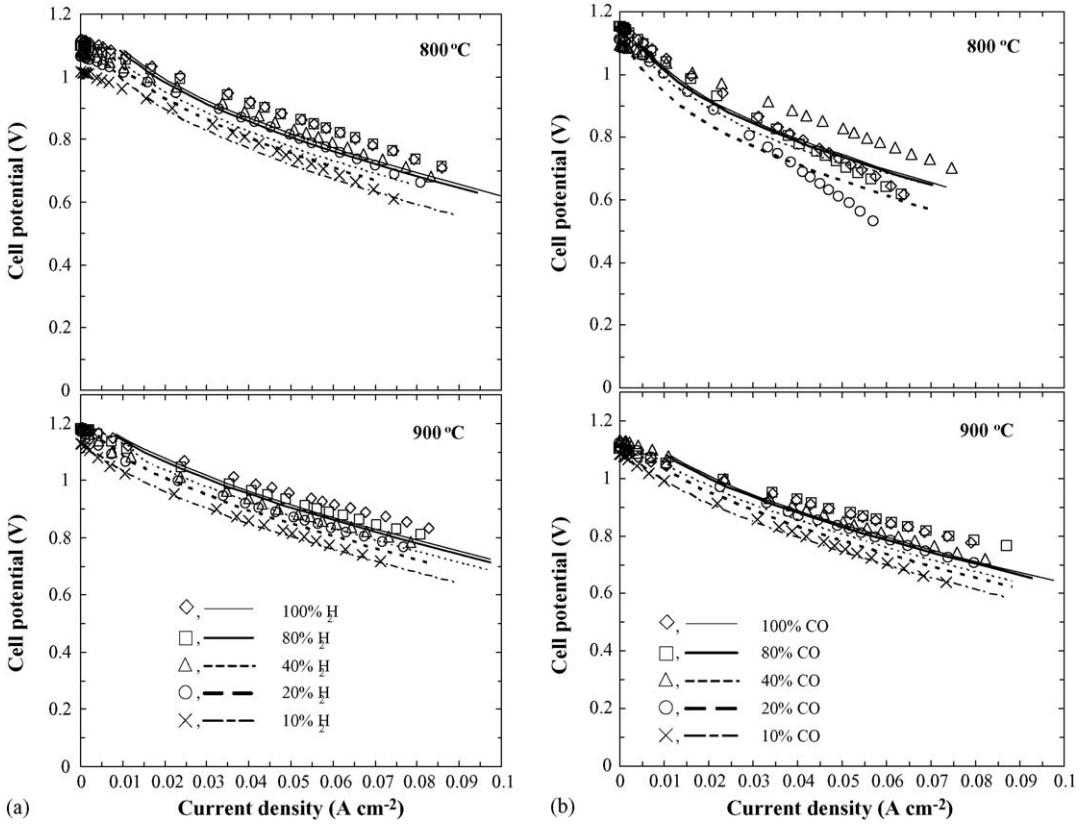

Fig. 4. Experimental (symbols) and predicted (lines) cell performances at various H_2/N_2 (a) and CO/N_2 (b) compositions at 800 and 900 °C for a fuel flow rate of 180 ml min^{-1}.

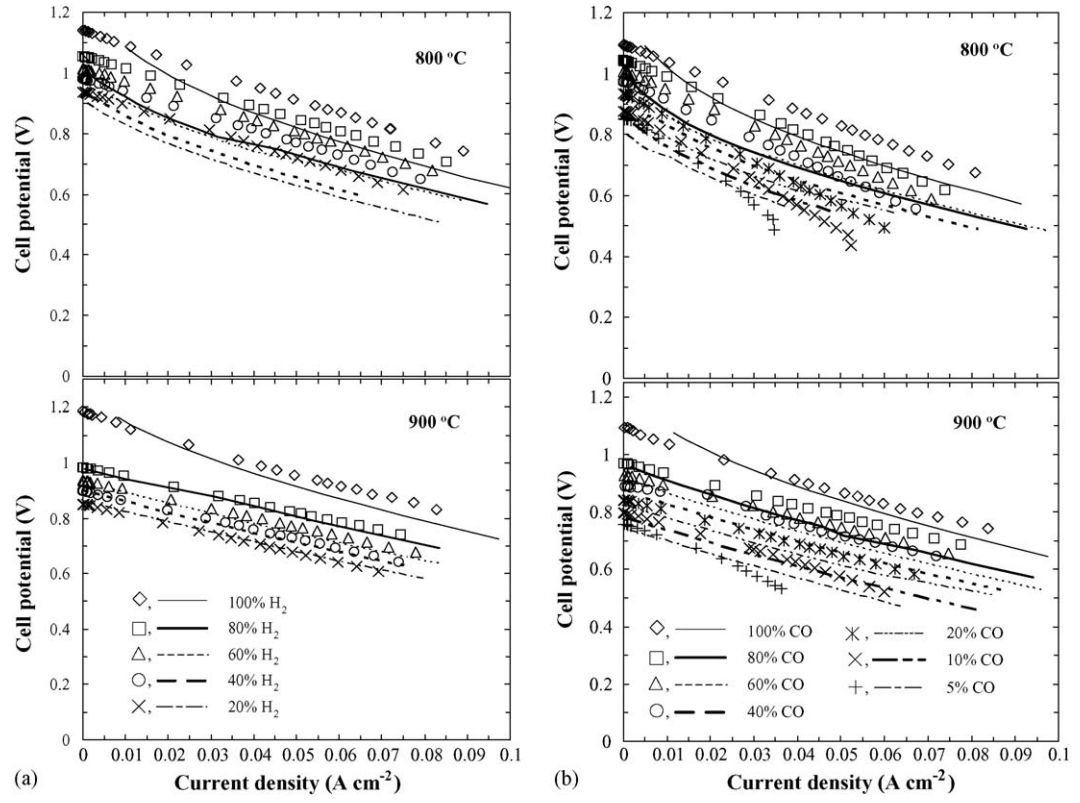

Fig. 5. Experimental (symbols) and predicted (lines) cell performances at various $H_2 + CO_2$ (a) and $CO + CO_2$ (b) compositions at 800 and 900 °C for a fuel flow rate of 180 ml min^{-1}.

total current density produced by H_2 and CO oxidation, i.e., $\vec{i} = -\sigma_e \partial\phi_e/\partial z = J_{H_2,an} + J_{CO,an}$. At the cathode/electrolyte interface at $z = z_c$, the molar flux of O_2 is given by $\vec{N}_{O_2} = -J_{cat}/4F$ and the current density $\vec{i} = -J_{cat}$.

3.6. Model calibration and numerical implementation

Before the cell performance could be modeled and validated against experimental data, it is necessary to account for the effect of the contact resistance at the current collector/electrode and electrode/electrolyte interfaces. The following approach is used. For each simulation, the cell potential, $\phi_{cat} - \phi_{an}$, is fixed to an arbitrary value and the model equations solved to yield the current density distribution along each electrode. The average current density along each electrode is then determined from this distribution, i.e.,

$$I_{avg} = 2r_b^{-2} \int_0^{r_b} r(J_{H_2,an} + J_{CO,an})\,dr \quad (27)$$

Since the model does not explicitly account for the contact resistances $R_{contact}$ in the cell, the actual potential, $V_{delivered}$, delivered to the external load is estimated as

$$V_{delivered} = (\phi_{cat} - \phi_{an}) - I_{avg} R_{contact} \quad (28)$$

The value of $R_{contact}$ is determined by calibrating the model to experimental data using the following procedure. A cell performance curve at a given set of gas flow rates was determined by measuring $V_{delivered}$ to an external load at different set values of the load resistance. This permitted the corresponding I_{avg} over the SOFC to be obtained and a performance plot of $V_{delivered}$ versus I_{avg} to be drawn. The model was calibrated against experimental data using pure H_2 as the fuel at temperatures of 800 and 900 °C. The value of $R_{contact}$ was obtained by fitting the $V_{delivered} - I_{avg}$ plot computed according to Eq. (28) to the experimentally observed one for the same operating conditions. Since $R_{contact}$ varies only with temperature, the values obtained at the two temperatures are then used in the subsequent simulations at the various syngas compositions.

The finite element software, *FEMLAB*® version 3.0 [30] was employed to solve the system of equations. The number of mesh elements in solving this model are around 4000 elements. Depending on the initial guesses, each simulation required between 2 and 5 min for completion on a Pentium IV 1.4 GHz with 1 GB RAM.

4. Results and discussion

4.1. Experimental results and model validation

The cell performances obtained from the model for various syngas compositions are compared with the experimental data at 800 and 900 °C first to obtain $R_{contact}$ and then to validate the model for other operating conditions. The model input parameters and operating conditions used in the model are summarized in Table 2. The cell potential was varied from 0.5 to 1.0 V by setting $\phi_{cat} = 0$ and varying ϕ_{an} from −0.5 to −1.0 V.

4.1.1. Effect of fuel flow rate

The comparison between model and experimental data using pure H_2 as fuel at various flow rates for cell operation at 800 and 900 °C is presented in Fig. 3. The fitting procedure yields $R_{contact}$ of 1.6 and 1.2 Ω cm^2 at 800 and 900 °C, respectively, which are in the range reported by Jiang [31].

As evident from Fig. 3, the cell potential during operation at 900 °C is slightly greater than that obtained at 800 °C. This occurs because the open-circuit is higher and the overpotentials are lower at the higher temperature. The model curves slightly underestimate the experimental data at 800 °C while they fit quite well at 900 °C. They also indicate that cell performance is independent of fuel flow rate, whereas the measured values show a small enhancement in cell performance at higher flow rates. This effect is more apparent at the lower temperature. For instance, at 800 °C and 0.05 A cm^{-2}, the cell potential increases from ∼0.86 to ∼0.9 V when the fuel flow rate is raised from 100 to 180 ml min^{-1}. A similar effect was reported by Cunningham et al. [32].

4.1.2. Effect of N_2 dilution

Fig. 4 shows experimental and predicted cell performances with $H_2 + N_2$ and $CO + N_2$ mixtures in which the H_2 (or CO) composition was varied from ∼100% to ∼10% at both 800 and 900 °C. The fuel flow rate is fixed at 180 ml min^{-1} in all cases. The model predictions agree well with the experimental data particularly at 900 °C. The experimental results in Fig. 4a show that the cell potential improves as H_2 concentration increases although the OCPs are similar. The model simulations indicate that one reason for this effect is that N_2 acts as an inert gas to the diffusion of H_2 from the bulk to the anode. Consequently, H_2 is less evenly distributed over the electrode. In addition, from a thermodynamic point of view, a higher partial pressure of H_2 leads to a higher cell potential. However, the impact of N_2 dilution is modest and the cell performance decreases by about 15% when the H_2 concentration is reduced from ∼100% to ∼10%.

When CO is diluted with N_2 at 800 °C (Fig. 4b), the OCP is similar to that for the $H_2 + N_2$ mixture with the same fuel gas composition, but the cell performance is lower. On the other hand, the cell performances using $CO + N_2$ and $H_2 + N_2$ mixtures are much closer to each other at 900 °C.

Considerable discrepancies between the model results and experimental data are observed at 800 °C (Fig. 4b), particularly at high current density and low CO concentration. The overestimation of cell performance by the model is likely due to the effect of carbon formation via the Boudouard reaction that is not considered in the model. Carbon formation is, of course, possible when CO is used as fuel and most likely at low current density when p_{CO} remains relatively high and p_{CO_2} is low. Each of the experimental performance curves in this study was obtained by varying the current density from low to high values using the same electrodes without disassembling the apparatus. Since carbon is not easily removed once formed [33], it is likely that some carbon formed at low current density remained on the anode when higher current densities were applied and continued to reduce cell performance.

Table 3
Fuel compositions due to the WGSR at 900 °C for various H_2/CO_2 mixtures

Inlet composition (%)		Fuel composition at SOFC anode (%)				E^0_{cell}
H_2	CO_2	H_2	CO	CO_2	H_2O	
99	0	99	0	0	1	1.15
80	20	63.3	16.7	3.3	17.7	0.98
60	40	34.4	25.6	14.4	26.6	0.93
40	60	14.4	24.5	34.4	26.6	0.89
20	80	3.3	16.7	63.3	17.7	0.83

4.1.3. Effect of CO_2 dilution

Fig. 5 shows experimental and predicted cell performances using $H_2 + CO_2$ and $CO + CO_2$ mixtures at both 800 and 900 °C. The composition of H_2 and CO was varied over the range from 100% to 10% in each of these mixtures. The effect of CO_2 dilution is more pronounced than that of N_2 dilution. The cell performance with H_2 (or CO) + CO_2 is lower than that with H_2 (or CO) + N_2 for the same fuel concentration. The OCP decreases significantly as CO_2 concentration is increased when either H_2 or CO is the fuel. As shown in Fig. 5a, the OCP at 800 and 900 °C decreases by 20% and 26%, respectively as H_2 concentration is decreased from 100% to 20%. This is likely due to the impact of the WGSR. For the $H_2 + CO_2$ mixture, the WGSR strongly influences the equilibrium compositions by converting some of H_2 and CO_2 to H_2O and CO which leads to a lower OCP, as indicated by Eqs. (17) and (22). The effect of CO_2 dilution on the OCP at 900 °C is summarized in Table 3.

From Fig. 5b, it is evident that at high CO concentration (~40% to ~100%) the same trends of experimental and model predicted cell performances are observed at both 800 and 900 °C. Unfortunately, the model slightly underestimates the experimental cell performance at both temperatures. On the other hand, the experimental cell potentials at low CO concentrations (~5% to ~20%) show a drop at high current densities that is not predicted by the model especially at 800 °C. These discrepancies are also likely caused by carbon formation on the anode.

4.1.4. Effect of H_2/CO composition

Fig. 6 shows the experimental and predicted cell performances for H_2/CO ratios diluted with 70% N_2 to reduce the rate of carbon formation that depends on the CO concentration in the fuel gas. The model only slightly underestimates the measured performance data at both temperatures. The OCP is essentially independent of the relative proportions of H_2 and CO. Moreover, the cell performance achieved when CO is the only oxidizable gas is slightly lower than that obtained when H_2 is the only fuel. This means that even though the CO oxidation rate is less than the H_2 oxidation rate, it has only a small impact on the relative cell performance. The main reason for this is that the cathodic overpotential plays a larger role on the cell performance than the anodic overpotential [33].

4.1.5. Effect of simulated syngas composition

In order to evaluate the ability of the model to predict cell performance with syngas fuel, model predictions were compared to experimental results obtained using various gas compositions.

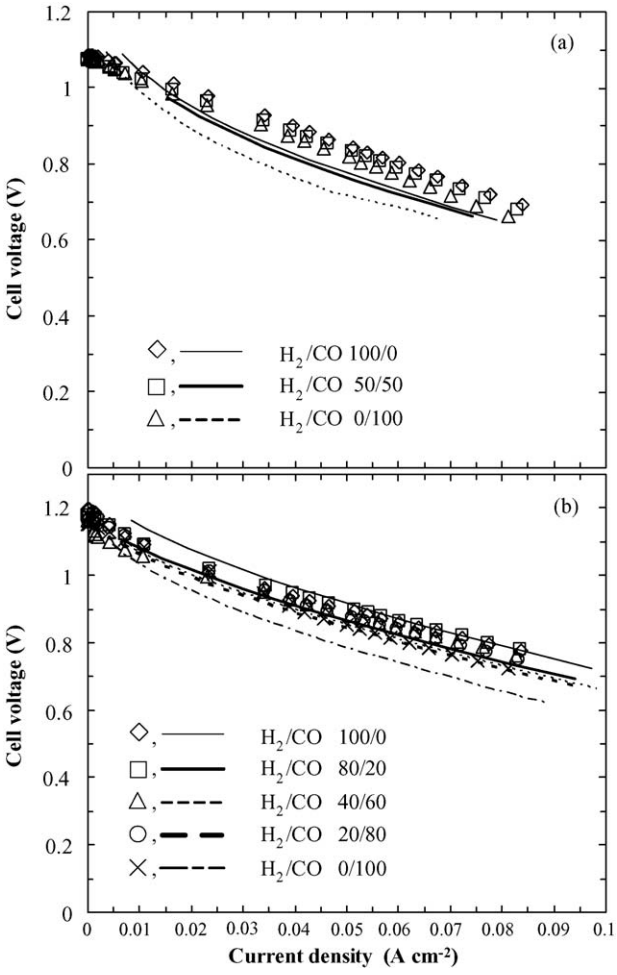

Fig. 6. Experimental (symbols) and predicted (lines) cell performances at various H_2/CO compositions diluted with 70% N_2 at (a) 800 °C and (b) 900 °C for a fuel flow rate of 180 ml min^{-1}.

The gas compositions used in these experiments are listed in Table 4.

Experimental and predicted cell performances for various syngas compositions at 800 and 900 °C are presented in Fig. 7. The predictions agree well with the experimental data at 900 °C, but underestimate the data at 800 °C although there is close agreement with regard to the OCP.

Fuel F1 consisting of moist H_2 provides the highest performance. However, it is interesting to note that fuel F6 which is a mixture of 20% H_2, 20% CO and 60% N_2 performs slightly bet-

Table 4
Simulated syngas composition

Fuel no.	Gas composition				
	H_2	H_2O	CO	CO_2	N_2
F1	97	3	–	–	–
F2	20	3	–	–	80
F3	20	3	–	14	66
F4	20	3	20	14	43
F5	32	3	45	15	3
F6	20	3	20	0	57

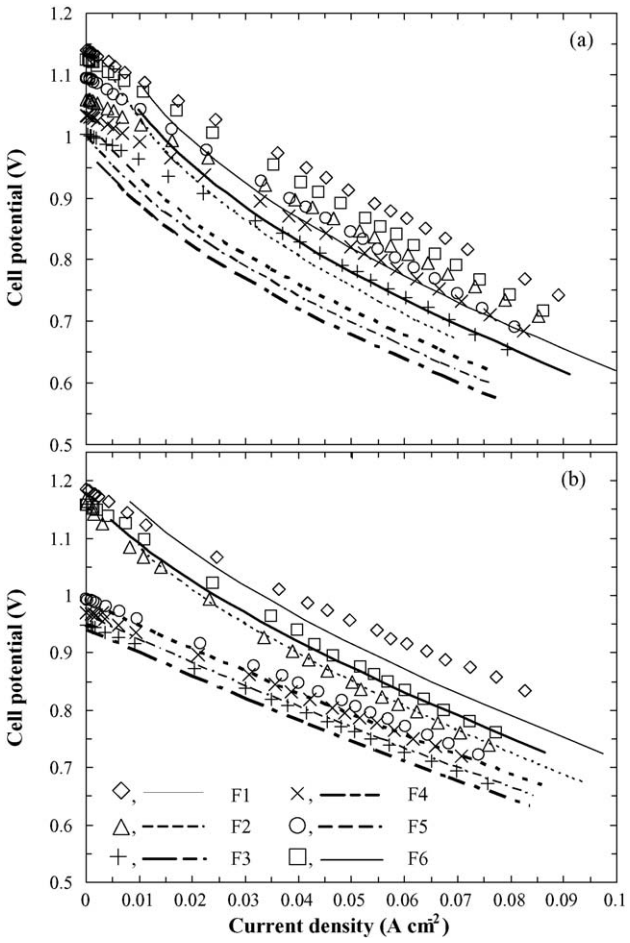

Fig. 7. Experimental (symbols) and predicted (lines) cell performances for simulated syngases at compositions summarized in Table 4 at (a) 800 °C and (b) 900 °C for a fuel flow rate of 180 ml min^{-1}.

ter than moist H_2 diluted by 80% N_2 (F2). This indicates that CO should be a useful fuel for SOFCs. Fuel F3 is a mixture of H_2, CO_2 and N_2, whereas F4 and F5 are examples of syngas compositions typically obtained from air and oxygen gasifiers [34], respectively. The OCPs obtained using F3, F4 and F5 are less than those of F1, F2 and F6, likely due to the effect of the WGSR in the presence of CO_2, as previously described. The cell performance using the F5 fuel is slightly greater than that using F4 because of the higher fuel content and lower N_2 dilution. However, when the cost of syngas production is considered, the use of syngas composition F4 may be the most economical choice. F3 yields the poorest cell performance because of its low fuel content and considerable dilution by presence of CO_2 and N_2. If CO_2 is removed before the syngas enters the SOFC, the cell performance could be further increased. On the other hand, the presence of CO_2 helps prevent carbon formation on the anode. Thus, a trade-off must be made to maximize cell performance and anode durability.

4.1.6. Cell inspection after operation

Once an experiment was completed at each operating temperature, the test rig was disassembled and the electrochemical cell visually inspected. A significant amount of Ni and carbon was found to have deposited on the anode current collector after operation at 800 °C, as confirmed by XRD analysis. Decolouration of the anode surface indicating Ni depletion was also noted. A thick layer of carbon was also observed in the anode feed entrance region of the cell.

On the other hand, only a small part of the Ni anode material delaminated and deposited on the anode current collector after cell operation at 900 °C. No evidence of carbon was found at the anode current collector or the anode surface and only a small amount was observed at the anode feed entrance region.

SEM images of anode surfaces obtained after operation at 800 and 900 °C are presented in Fig. 8. The anode surface obtained at 800 °C appears to be worse than that obtained at 900 °C. The anode surface at the lower temperature has become almost completely deactivated due to the presence of many particles that block the pores and prevent reactant gases from reaching the active sites within the pores. Those particles are should be composed of Ni delaminated from the anode surface. Furthermore, the pore size after operation at 800 °C appears smaller than that at 900 °C likely due to Ni agglomeration.

From visual and SEM investigation, anode delamination appears to be related to carbon formation which deteriorates cell performance. The actual mechanism of anode delamination due to carbon formation has not been clearly established. However, the role of Ni used in an SOFC anode is likely similar to that in Ni-supported catalysts. A mechanism for Ni disintegration from its support due to carbon formation on Ni-supported catalysts has been proposed by Snoeck et al. [35]. According to this explanation, the Boudouard reaction leads to the adsorption of carbon atoms onto the catalyst which then dissolve into the

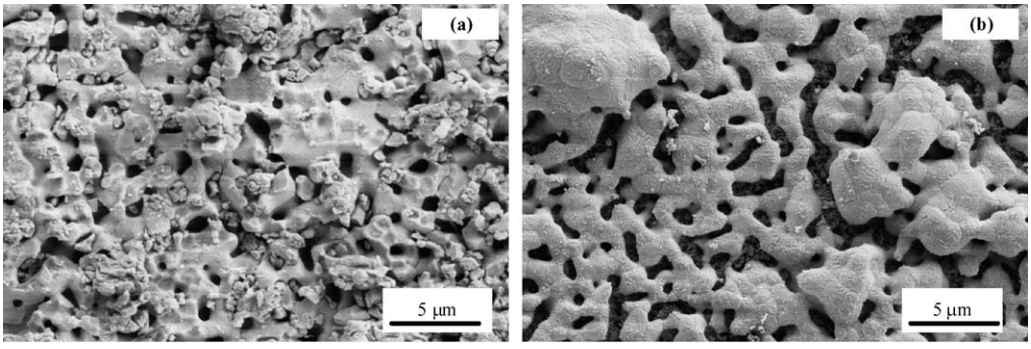

Fig. 8. SEM images of anode surface obtained after operation at 800 °C (a) and 900 °C (b).

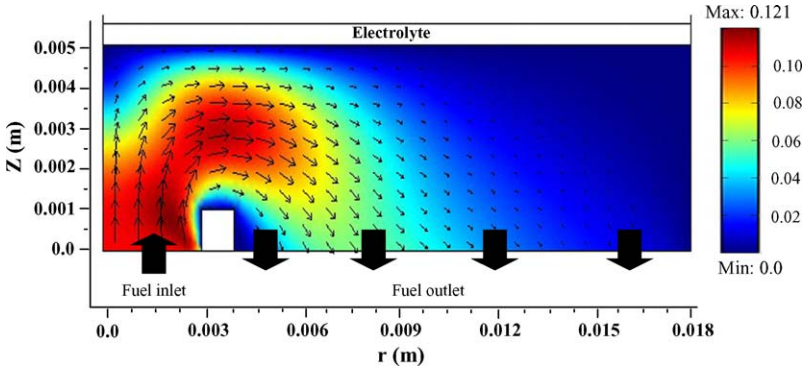

Fig. 9. Surface and arrow plots showing the velocity field inside fuel channel for the base case conditions.

nickel on the gas side and diffuse through the Ni particle to the support side, which eventually causes the separation of Ni from the support leading to nucleation of carbon filaments.

4.2. Simulation results for simulated syngas

The simulation results discussed here are based on simulated syngas obtained from biomass gasification in air (fuel F4 in previous section). The operating conditions are summarized in Table 5. It is noted here that the contact resistance is assumed to be zero for the purposes of this simulation.

The velocity field inside the fuel channel for the base case conditions is depicted in Fig. 9. The velocity is high at the entrance region and is reduced as one moves away from the entrance. Since the feed tube is much smaller than the fuel channel, uneven flow occurs as the fuel gas is dispersed from the feed tube to the fuel channel. Once the fuel gas reaches the anode surface, it begins to flow in the reverse direction toward the discharge from the fuel channel. It is found that the gas velocity is almost zero near the edge of the fuel channel ($r_b = 0.018$ m). Accordingly, transport of the gases in this region occurs primarily by diffusion and eventually local current density in this area as illustrated in Fig. 10. Therefore, reactant concentrations (H_2 and CO) at the edge of the fuel channel are less than those in the fuel channel close to the feed tube.

The distributions of the H_2, CO, CO_2, H_2O concentrations inside the fuel channel are displayed in Fig. 10. The H_2 concentration declines sharply as the gas moves through the fuel inlet region and then decreases more gradually in the region further away from the fuel inlet. This is due to its high rate of consumption by electrochemical oxidation and the WGSR to produce CO and H_2O on the portion of the anode near the inlet. This is confirmed in Fig. 10c that shows the CO concentration rising at the anode surface near the fuel inlet. Once the WGSR reaches equilibrium, H_2 is mainly consumed by electrochemical oxidation which is slower than the WGSR, leading to a more uniform concentration. The H_2O concentration increases abruptly at the fuel inlet region due to the WGSR. This also causes the concentration profiles of CO and CO_2 in fuel inlet region to be inverted with respect to one another.

Table 5
Base case operating conditions

Operating condition	Value
Pressure	1 atm (101.35×10^5 Pa)
Temperature	900 °C
Fuel flow rate	180 ml min^{-1}
Fuel gas composition (fuel, F4)	20% H_2, 20% CO, 14% CO_2 and 3% H_2O, 43% N_2
Cathodic half-cell potential (ϕ_{cat})	0 V
Anodic half-cell potential (ϕ_{an})	−0.7 V
Oxidant	Air
Contact resistance ($R_{contact}$)	0 Ω cm^{-2}

As shown in Fig. 11, the oxygen concentration distribution remains uniform throughout the air channel. This implies that sufficient amount of O_2 is being transferred to the cathode surface even if its source is ambient air. Therefore, the use of an air feed tube is not necessary in this set-up.

The distributions of the total current density and the partial current densities due to H_2 and CO oxidation along the electrode surface are shown in Fig. 12. These show that the current density gradually decreases along the length of the anode surface. The rate of H_2 oxidation remains about 2.5 times greater than that of CO oxidations, as specified by the electrochemical kinetic expressions, although the diffusivity of CO is much less than that of H_2 (Table 2). This indicates that the influence of mass transport along the anode surface is not significant.

The breakdown of the overpotentials along both electrodes is shown in Fig. 13. All overpotentials are quite uniform along the electrode surface due to the uniform current density distribution. The cathodic overpotential (η_{cat}) is about two times larger than the other overpotentials. The ohmic overpotential (η_Ω), anodic overpotential for H_2 oxidation ($\eta_{H_2,an}$) and anodic overpotential for CO oxidation ($\eta_{CO,an}$) are very similar in magnitude. Since the cathodic overpotential is large and not dependent on the H_2/CO ratio, the cell potential is not affected by the H_2/CO ratio, as observed in Fig. 6.

4.3. Thermodynamic analysis of carbon formation on an SOFC anode

As discussed previously, the possibility of carbon formation is based on whether the carbon activity ratio $\alpha_C = K_{eq,B} p_{CO}^2 / p_{CO_2}$ obtained from the model exceeds 1.0 (Eq. (26)). This calculation accounts for the influences of the electrochemical oxidation of H_2 and CO, operating temperature, pressure

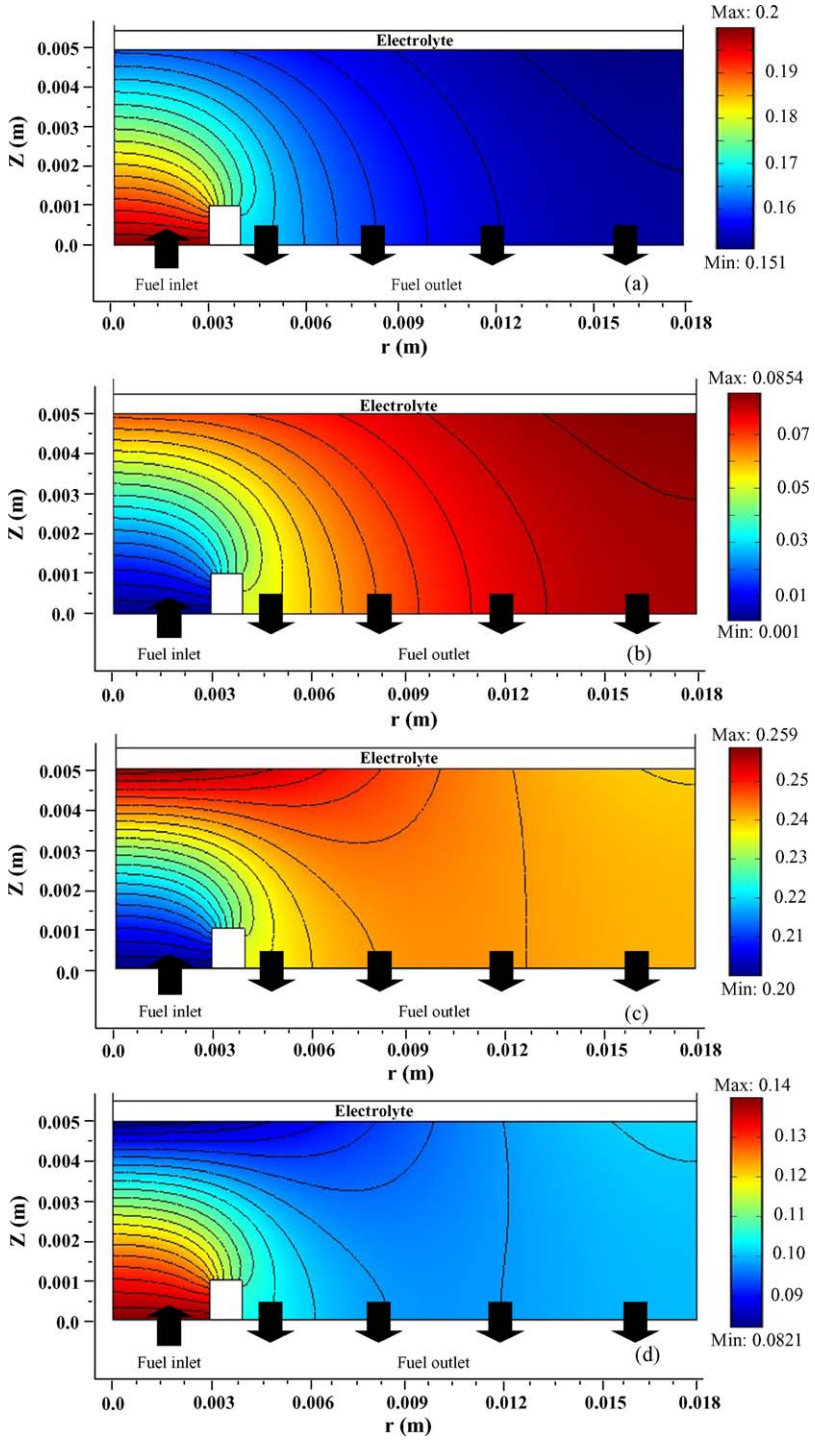

Fig. 10. Surface and contour plots of concentrations for H_2 (a); H_2O (b); CO (c) and CO_2 (d) inside fuel channel.

and inlet syngas composition. R_{contact} has been set to zero for the purposes of these calculations. The effect of the CO content and current density on the carbon activity ratio for cell operation at 800 and 900 °C is depicted in Fig. 14. The value of the carbon activity ratio shown is the average of the local values computed along the anode surface. i.e.,

$$\alpha_{\text{c,ang}} = 2r_{\text{b}}^{-2} \int_0^{r_{\text{b}}} r\alpha_{\text{c}}(r)\,\mathrm{d}r \tag{29}$$

The CO content is defined as

$$\text{CO content} = \frac{\text{mole fraction of CO}}{\text{mole fraction of CO} + \text{mole fraction of H}_2} \tag{30}$$

The inlet fuel stream is assumed to contain no H_2O and CO_2.

Fig. 14 indicates that the CO content and current density have a significant impact on the possibility of carbon formation (i.e., $\alpha_C > 1$) for cell operation at 800 °C. In contrast, carbon forma-

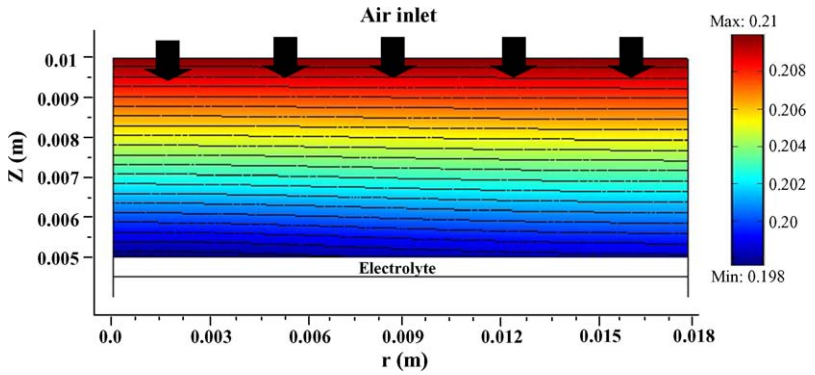

Fig. 11. Surface and contour plots of O_2 concentration inside air channel.

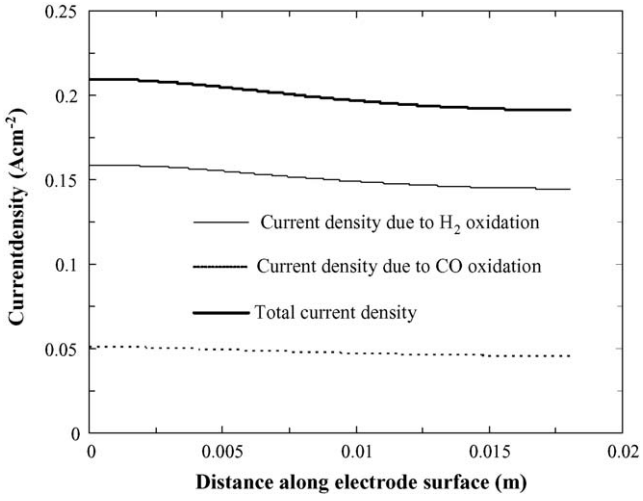

Fig. 12. Current density distributions along electrode surface.

tion can be avoided at 900 °C over the entire range of current density and CO contents because of the lower equilibrium constant for the Boudouard reaction at the higher temperature. This difference agrees with the experimental observations described in Section 4.1.6. Nonetheless, operation at 800 °C or below is potentially more attractive because of the wider choice of mate-

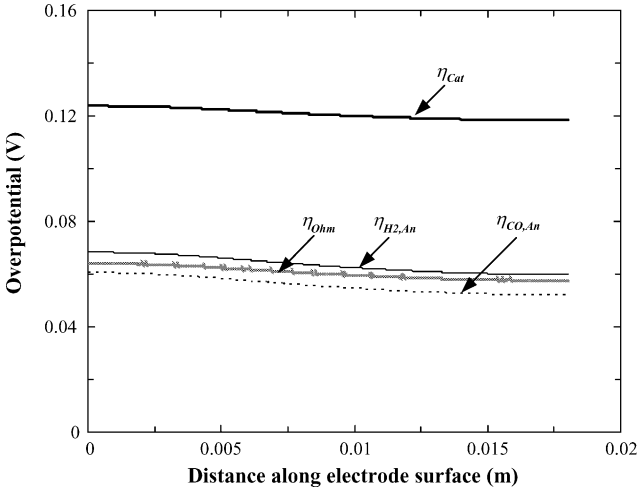

Fig. 13. Break down of overpotentials along electrode surface.

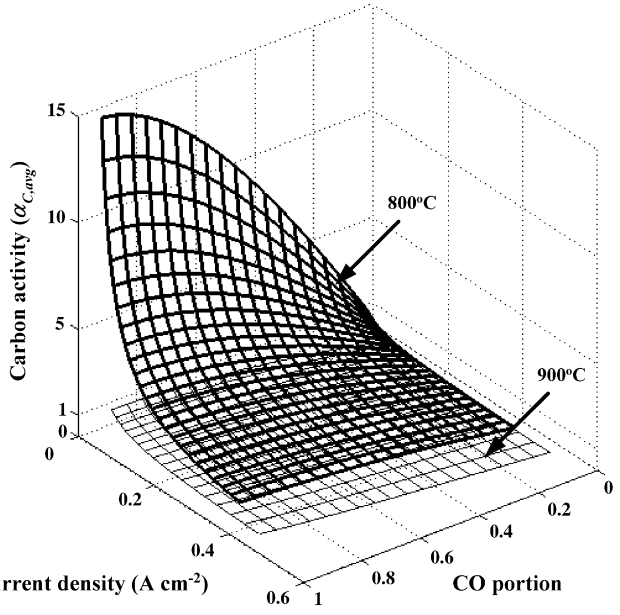

Fig. 14. Effects of current density and CO content on carbon activity at 1 atm and 800 and 900 °C.

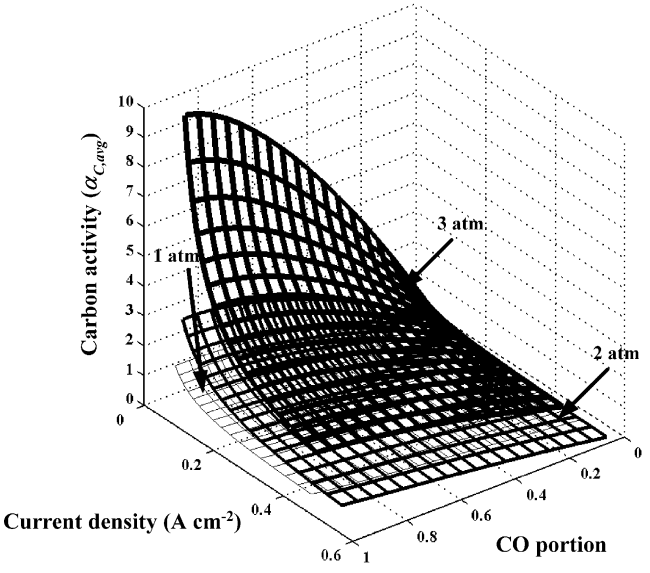

Fig. 15. Effects of current density and CO content on carbon activity at 900 °C and various operating pressures.

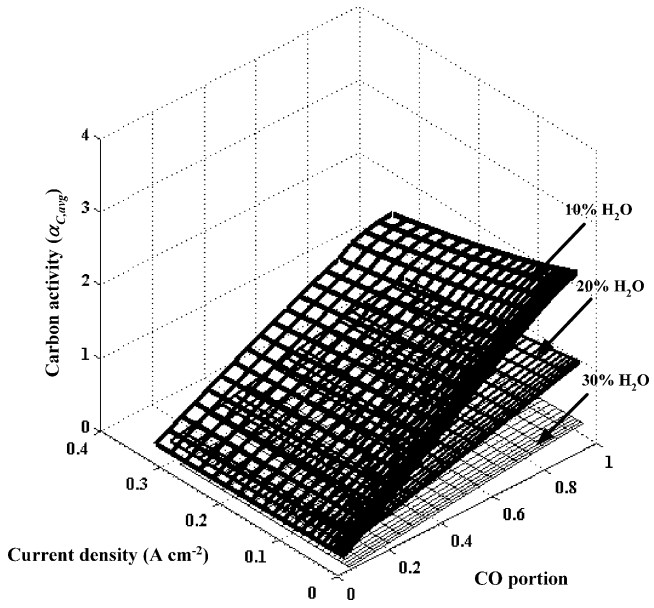

Fig. 16. Effects of current density and CO content on carbon activity at 800 °C, 3 atm and various H_2O compositions.

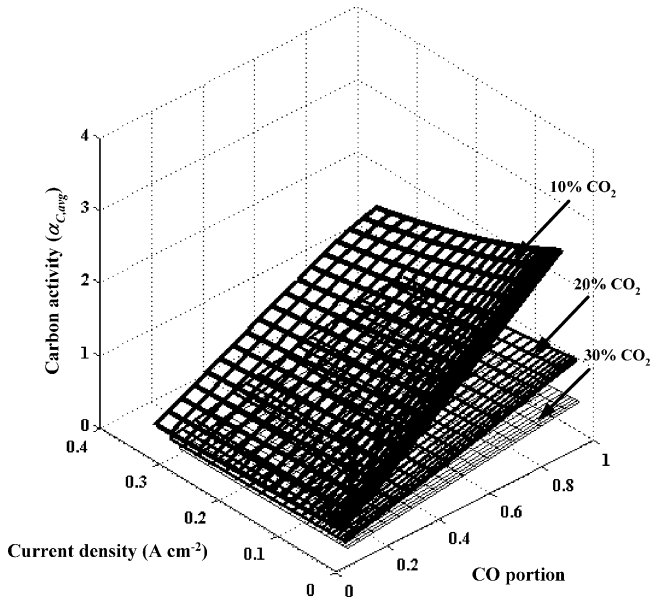

Fig. 17. Effects of current density and CO content on carbon activity at 800 °C and 3 atm and various CO_2 compositions.

rials that can be used for cell components. It is also observed that likelihood of carbon formation at 800 °C can be reduced by operating at higher current density and lower CO content. An increase in current density enhances the rate of H_2 and CO oxidation and the rate of H_2O and CO_2 production. Thereafter, H_2O reacts with CO via the WGSR to form more CO_2 and H_2. These effects tend to reduce at lower α_C.

In actual SOFC operation, syngas fuel typically contains about 50–60% CO. Therefore, according to Fig. 14, the cell should be operated at a minimum of 0.1 A cm^{-2} to ensure that enough CO_2 and H_2O are generated to prevent carbon formation at 800 °C. However, it should be noted that this calculation is based on a syngas containing only H_2 and CO. If the inlet syngas composition contains H_2O and/or CO_2, operation of a lower current density than 0.1 A cm^{-2} might be possible because their presence helps to prevent carbon formation, as will be described later.

Fig. 15 displays the effects of current density and CO content on the carbon activity ratio at various operating pressures and 900 °C. An increase in operating pressure favours carbon formation, especially at high CO content and low current density. Operation at 3 atm has the danger of forming carbon over the entire range of operating current densities and CO contents. The application of such a pressure has recently received attention due to the proposal for the use a SOFC/micro-turbine hybrid cycle which has a high overall efficiency, but requires a high inlet pressure for the micro-turbine.

As previously described, an operating target of 800 °C and 3 atm would be ideal. Unfortunately, these conditions can lead to unreliable and low cell performance due to carbon formation. One of the possible ways to reduce this likelihood is to increase the amount of H_2O and CO_2 in the inlet stream. The effects of the current density and CO content on α at various inlet H_2O and CO_2 compositions at 800 °C and 3 atm are shown in Figs. 16 and 17, respectively. The likelihood of carbon formation is substantially decreased by increasing H_2O or CO_2 concentration in the inlet stream especially at high CO content. A syngas fuel containing 50–60% CO content requires at least 20% H_2O or CO_2 concentration to reduce the risk of carbon formation during operation. Unfortunately, cell power will slightly be reduced since this tends to lower the OCP.

5. Conclusions

A mechanistic model based on a button cell geometry is validated against experimental performance data at 800 and 900 °C. This comparison shows that the model agrees reasonably well with the experimental data at 900 °C but not as well in the case of 800 °C.

The experimental data and the model simulations indicate that the major reason for achieving lower cell performance when the SOFC operates with syngas fuel is carbon formation via the Boudouard reaction that damages the anode surface. If this problem can be alleviated, then the analysis shows that CO is an effective fuel. CO_2 dilution has a more pronounced effect on the cell performance than that of N_2 because CO_2 significantly reduces OCP. A thermodynamic analysis of carbon formation shows that the operating pressure, temperature and inlet H_2 and CO compositions are important factors. The operation of SOFCs at intermediate temperature and high pressure with syngas is limited by carbon formation. However, this may be overcome by adding H_2O or CO_2 into the syngas fuel, although at the expense of some loss in the electric power delivered by the fuel cell.

Acknowledgements

Financial support from CANMET Energy Technology Centre (CANMET) and CO_2 consortium, Canada, and the National

Metals and Materials Technology Center (MTEC), Thailand, is gratefully acknowledged. R.S. also extends special thanks to Dr. Suttichai Assabumrungrut and Dr. Navadol Laosiripojana for their helpful discussions and to the fuel cell researchers at MTEC for helping set up the experiments.

References

[1] US DOE, Fuel Cell Handbook, EG&G Services Inc., West Virginia, 2000, pp. 8–15.
[2] K. Hassmann, Fuel Cells 1 (2001) 78.
[3] S. Onuma, A. Kaimai, K. Kawamura, Y. Nigara, T. Kawada, J. Mizusaki, H. Tagawa, Solid State Ionics 132 (2000) 309.
[4] Y. Matsuzaki, M. Hishinuma, I. Yasuda, in: S.C. Singhal, M. Dokiya (Eds.), Proceedings of Solid Oxide Fuel Cell VI, PV 99-19, The Electrochemical Society Proceedings Series, Pennington, NJ, 1999, p. 560.
[5] K. Eguchi, H. Kojo, T. Takeguchi, R. Kikuchi, K. Sasaki, Solid State Ionics 152/153 (2002) 411.
[6] A. Weber, B. Sauer, A. Muller, D. Herbstritt, E. Ivers-Tiffe, Solid Sate Ionics 152/153 (2002) 543.
[7] K. Sasaki, Y. Hori, R. Kikuchi, K. Eguchi, A. Ueno, H. Takeuchi, M. Aizawa, K. Tsujimoto, H. Tajiri, H. Nishikawa, Y. Uchida, J. Electrochem. Soc. 149 (2002) A227.
[8] S. Baron, N. Brandon, A. Atkinson, B. Steele, R. Rudkin, J. Power Sources 126 (2004) 58.
[9] S.H. Chan, K.A. Khor, Z.T. Xia, J. Power Sources 93 (2001) 130.
[10] C. Kleinstreuer, Engineering Fluid Dynamics, Cambridge University Press, Cambridge, United Kingdom, 1997.
[11] R.R. Bird, W.E. Stewart, E.N. Lightfoot, Transport Phenomena, John Wiley & Sons, NY, 1960.
[12] D.R. Crow, Principles and Applications of Electrochemistry, 4th ed., Chapman & Hall, New York, USA, 1994.
[13] A.S. Loselevich, A.A. Kornyshev, Fuel Cells 1 (2001) 40.
[14] A. Sawata, K. Tsuneyoshi, J. Mizusaki, H. Tagawa, Solid State Ionics 40/41 (1990) 415.
[15] S. Nagata, A. Momma, T. Kato, Y. Kasuga, J. Power Sources 101 (2001) 60.
[16] E. Achebach, J. Power Sources 49 (1994) 333.
[17] P. Costamagna, K. Honegger, J. Electrochem. Soc. 145 (1998) 3995.
[18] T. Setoguchi, K. Okamoto, K. Eguchi, H. Arai, J. Electrochem. Soc. 139 (1992) 2875.
[19] Y. Jiang, A.V. Virkar, J. Electrochem. Soc. 150 (2003) A942.
[20] Y. Matzusaki, M. Hishinuma, I. Yasuda, in: S.C. Singhal, M. Dokiya (Eds.), Proceedings of Solid Oxide Fuel Cell VI, PV 99-19, The Electrochemical Society Proceedings Series, Pennington, NJ, 1999, p. 560.
[21] B.A. Haberman, J.B. Young, Int. J. Heat Mass Trans. 4 (2004) 3617–3629.
[22] P. Aguiar, C.S. Adjiman, N.P. Brandon, J. Power Sources 138 (2004) 120.
[23] J.R. Ferguson, J.M. Fiard, R. Herbin, J. Power Sources 58 (1996) 109.
[24] P.W. Li, M.K. Chyu, J. Power Sources 124 (2003) 487.
[25] K. Ahmed, K. Föger, J. Power Sources 103 (2001) 150.
[26] S.H. Clarke, A.L. Dicks, K. Pointon, T.A. Smith, T. Swann, Catal. Today 38 (1997) 411–423.
[27] S.L. Douvartzides, F.A. Coutelieris, A.K. Demin, P.E. Tsiakaras, AIChE J. 49 (2003) 248.
[28] S. Assabumrungrat, V. Pavarajarn, S. Charojrochkul, N. Laosiripojana, Chem. Eng. Sci. 59 (2004) 6015.
[29] S. Assabumrungrat, N. Laosiripojana, V. Pavarajarn, W. Sangtongkitcharoen, A. Tangjitmatee, P. Praserthdam, J. Power Sources 139 (2005) 55.
[30] COMSOL Ltd., FEMLAB® Version 3.0 User's Guide, COMSOL, Boston, 2004.
[31] S.P. Jiang, J. Electrochem. Soc. 148 (2001) A887.
[32] R. Cunningham, R. Collins, G. Saunders, in: M. Morgensen (Ed.), Proceedings of Sixth European Solid Oxide Fuel Cell Forum, Lucerne, Switzerland, 2004, p. 309.
[33] J.-H. Koh, Y.-S. Yoo, J.-W. Park, H.C. Lim, Solid State Ionics 149 (2002) 157.
[34] G. Sridhar, P.J. Paul, H.S. Mukunda, Biomass Bioenergy 21 (2001) 61.
[35] J.W. Snoeck, G.F. Froment, M. Fowles, J. Catal. 169 (1997) 240.